

Resolved simulations of sedimenting suspensions of spheres

Daniel P. Willen^{1,*} and Andrea Prosperetti^{2,3,†}

¹*Department of Mechanical Engineering, Johns Hopkins University, 3400 North Charles Street, Baltimore, Maryland 21218, USA*

²*Department of Mechanical Engineering, University of Houston, 4726 Calhoun Road, Houston, Texas 77204-4006, USA*

³*Faculty of Science and Technology and J.M. Burgers Centre for Fluid Dynamics, University of Twente, P.O. Box 217, 7500 Enschede, Overijssel, Netherlands*



(Received 22 June 2018; published 18 January 2019)

Several results on sedimenting equal spheres obtained by resolved simulations with the Physalis method are presented. The volume fraction ranges from 8.7% to 34.9% and the particle Galilei number from 49.7 to 99.4. The results shown concern particle collisions, diffusivities, the mean free path, the particle pair distribution function, and other features. It is found that many qualitative trends found in earlier studies continue to hold in the parameter range investigated here as well. The analysis of collisions reveals that particles interact prevalently via their flow fields rather than by direct contacts. A tendency toward particle clustering is demonstrated. The time evolution of the shape and size of particle tetrads is examined.

DOI: [10.1103/PhysRevFluids.4.014304](https://doi.org/10.1103/PhysRevFluids.4.014304)

I. INTRODUCTION

The importance of fluids with suspended settling particles in natural and engineering systems such as sedimentation, fluidized beds, sediment transport, and many others has motivated numerous experimental, theoretical, and computational studies. Theoretical progress is hampered by the inherent great complexity of the phenomenon, especially when effects due to a finite particle Reynolds number become significant. In this situation, particle-resolved numerical simulations and a detailed analysis of the results thereby obtained offer hope to gain the insight necessary for progress in the modeling of such systems.

Table I summarizes the parameter range covered by several experimental and numerical studies of sedimenting particles (labels E and N, respectively) [1–6]. The earlier papers focused on the Stokes regime. The advent of new numerical methods and more powerful computers has opened the way to the study of Reynolds number effects. By and large, in the parameter range where studies overlap, findings have been consistent. For example, the volume fraction dependence of the average settling speed has been found to be well correlated by the Richardson-Zaki expression [7,8] modified by a prefactor as suggested in later work (see, e.g., Refs. [9–11]). A larger velocity fluctuation amplitude in the vertical rather than the horizontal direction has been reported by many authors (see, e.g., [12,13]). Connections of these phenomena with the pair distribution function and its dependence on the particle volume fraction and particle Reynolds number have also been pointed out (see, e.g., [14]). The vexed question of the divergence of the velocity fluctuations with vessel size [15] has received much attention especially in the dilute low-Reynolds-number regime (see [16]

* daniel.willen@jhu.edu; <http://www.physaliscfd.org>

† aprosper@central.uh.edu

TABLE I. Parameter ranges addressed by some previous experimental and numerical studies (type labels E or N, respectively) of settling particles in a fluid. Here Ga is the Galilei number, ρ_p/ρ_f the particle-to-fluid density ratio, ϕ the particle volume fraction, and Re_t the single-particle terminal Reynolds number. When not explicitly given in the original reference, the Galilei number was calculated from (2).

Reference	Type	Ga	ρ_p/ρ_f	ϕ (%)	$Re_t = dw_t/\nu$
Ham and Homsy [34]	E	~ 0.04	2.24	2.5–10	$< 10^{-4}$
Nicolai <i>et al.</i> [25]	E	~ 0.1	2.53	0–40	$< 10^{-3}$
Segre <i>et al.</i> [1]	E	~ 0.05	~ 1	0.1–5	1.2×10^{-4}
Segre <i>et al.</i> [2]	E	0.04		5–50	10^{-4}
Chehata-Gomez <i>et al.</i> [3]	E	~ 0.03	2.6–4.2	0.1–0.8	$\sim 4 \times 10^{-5}$
Snabre <i>et al.</i> [4]	E	0.17	1.34	10–55	1.6×10^{-3}
Ladd [26]	N			5–45	0
Climent and Maxey [12]	N	1.4–17.9	0.9–1.5	1–12	0.1–10
Yin and Koch [11]	N	4.5–28.5	2.0	0.5–40	1–20
Yin and Koch [30]	N	1.9–28.5	2.0	1–20	0.2–20
Hamid <i>et al.</i> [5]	N	2.3	5	1–50	0.28
Hamid <i>et al.</i> [14]	N	1.0–17.9	5	1–40	0.05–10
Uhlmann and Doychev [27]	N	121, 178	1.5	0.5	141, 233
Zaidi <i>et al.</i> [13]	N	0.4–54.3	2.5–2.7	≤ 40	0.01–50
Fornari <i>et al.</i> [6]	N	145	1.02	0.5–1	188
present work	N	50–99	2.0–5.0	8.7–34.9	44–114

for a good summary). The matter has been resolved by showing that the predicted divergence only occurs with a hard-sphere particle distribution which in practice does not persist due to the evolution of the suspension microstructure, in particular with increasing Reynolds number.

These results are very helpful in that they begin to flesh out a picture of the dynamics of these systems. However, as can be seen from Table I, the region of parameter space covered by these studies is still limited, especially in view of the range relevant for many applications. In the present paper we use the Physalis numerical method (see, e.g., [17]) to examine many of the issues studied by previous investigators extending the parameter range, in particular by considering moderately dense suspensions at single-particle Reynolds numbers up to 114. In addition, we study particle collisions, clustering, and the time evolution of tetrads i.e., four-particle structures. We find that several earlier results on the two-particle distribution function, particle diffusivity, and particle velocity fluctuations hold also in the parameter range considered here. Several previously identified qualitative features of the results, such as trends with increasing volume fraction, are found not to be intrinsic to the system dynamics, but dependent on the normalization used to present the results. Additional information and two animations are presented in the Supplemental Material [18].

II. SIMULATIONS

The numerical simulations generating the data used for this paper have been described in some detail in an earlier publication [19] to which the reader is referred for details. Here we present a brief summary.

We carry out resolved simulations of equal spheres of radius a , diameter $d = 2a$, and density ρ_p suspended in an upward fluid flow. The pressure gradient driving the fluid is set in such a way that the mean settling velocity of the spheres vanishes. The computational domain is a parallelepiped with a horizontal cross section of dimensions $20a \times 20a$ and a vertical extent of $60a$; periodicity conditions are applied on all boundaries. With 500, 1000, 1500, and 2000 equal particles the mean particle volume fraction ϕ takes the values 8.7%, 17.5%, 26.2%, and 34.9%, respectively. According to [11], for volume fractions greater than 5% and domain sizes greater than ten particle

diameters, particle wakes are sufficiently disrupted by other particles that periodicity conditions do not introduce undesirable artifacts. We consider four different values of the particle-to-fluid density ratio $\rho_p/\rho_f = 2.0, 3.3, 4.0,$ and 5.0 .

The simulations are performed with the Physalis method, a complete description of which is available in several papers including, most recently, [17]; implementation details are described in [20]. The Navier-Stokes equations are solved on a fixed Cartesian grid by a projection method. The fluid-particle coupling is based on the fact that, in the vicinity of the no-slip particle surfaces, the fluid motion differs little from a rigid-body motion. This circumstance permits the Navier-Stokes equations to be linearized to the Stokes form, for which Lamb [21,22] obtained an exact solution in the form of a series. This analytical solution is used to transfer the no-slip condition holding at the particle surface to the closest Cartesian grid nodes, thus bypassing the difficulties deriving from the complex geometrical relationship between the spherical particles and the underlying Cartesian grid. We use eight mesh lengths per particle radius which, due to the spectral convergence of the Lamb solution and on the basis of earlier validations tests, are sufficient for an accurate resolution of the flow.

In addition to fluid-dynamic forces, obtained from the Physalis method, particles interact via lubrication and collision forces. The former are implemented by explicitly adding the analytical expressions available in the literature. The latter are implemented by means of a Hertzian contact model described in detail in [17]. To avoid the very stringent time step constraint required by the use of a realistic value of the particle Young's modulus, we used a fairly small value of this modulus, 0.65 MPa. The collisional Stokes number $St_c = \rho^* Re_r/9$, with Re_r the particle Reynolds number based on the relative velocity, characterizes the strength of the collisions (see, e.g., [23]). Typical values of St_c encountered in the present simulations were at most 10–20. Thus, collisions are dominated by the fluid viscosity and lubrication forces and are too weak to result in a rebounding motion of the colliding particles (see Fig. 6 in Ref. [17]). For this reason, the use of a smaller Young's modulus cannot affect the results in a significant way.

At each time step the particle position and orientation are updated on the basis of the calculated forces and couples of hydrodynamic origin, collisions, gravity, and buoyancy. Hydrodynamic forces and couples are found directly from the coefficients of the Lamb expansion with no need for additional calculation. The particle surface is sharp and the no-slip condition at the particle surface is satisfied to analytical accuracy whatever the level of truncation of the series in the Lamb solution. The simulations described in this work were carried out retaining 25 coefficients in the Lamb series, which corresponds to retaining multipoles up to and including order 2. The simulation parameters for $\rho_p/\rho_f = 3.3$ were chosen to match one of the experiments reported in [7] with glass beads in a liquid mixture.

In order to characterize the balance between gravity and viscous dissipation it is convenient to use the Galilei number

$$Ga = \frac{1}{\nu} \sqrt{\left(\frac{\rho_p}{\rho_f} - 1\right) d^3 g}, \quad (1)$$

in which g is the acceleration of gravity and ν the fluid kinematic viscosity; the values of Ga corresponding to the present simulations are shown in Table II. By carrying out separate simulations in domains with size $20a \times 20a \times 80a$ we have calculated the terminal settling velocity w_t of single particles for the density ratios used in this study. The results are shown in the form of the single-particle Reynolds number $Re_t = dw_t/\nu$ in Table II, together with the values of Re_t obtained from the empirical relation [11]

$$Ga^2 = \begin{cases} 18 Re_t [1 + 0.1315 Re_t^{0.82 - 0.05 \log_{10} Re_t}], & 0.01 < Re_t < 20 \\ 18 Re_t [1 + 0.1935 Re_t^{0.6305}], & 20 < Re_t < 260, \end{cases} \quad (2)$$

with the Galilei numbers used in the simulations. The numerical results and the values of Re_t that satisfy this correlation are found to be in very good agreement with each other.

TABLE II. Galilei number, single-particle Reynolds number Re_t from the present simulations, and values of Re_t that satisfy the correlation (2) from Ref. [11] for the four particle-to-fluid density ratios considered in this study.

ρ_p/ρ_f	Ga	Re_t	Re_t from Eq. (2)
2.0	49.7	43.27	44.17
3.3	75.4	76.60	78.40
4.0	86.1	91.57	93.82
5.0	99.4	110.8	113.7

Particles were initially randomly arranged in the computational domain and, before data were recorded, allowed to reach a statistically steady state as revealed by the average values of the fluid velocity and particle velocity fluctuations. For the lower densities and volume fractions we could run the simulations up to dimensionless times $\nu t/d^2 = 24.3$. However, as the density ratio and volume fraction increase, interparticle interactions become more frequent and energetic, which requires a smaller time step and more iterations for convergence. In these cases, for practical reasons, we only integrated up to $\nu t/d^2$ of about 14.2. Due to computational constraints, we were unable to run some simulations at the higher volume fractions and density ratios.

III. RESULTS

The present simulations are conducted in the frame of reference in which the mean vertical particle velocity $\langle w_z \rangle$ vanishes at each time step; here the angular brackets denote the average over the particles. Thus, the frame of reference used here is appropriate for the description of a fluidized-bed-like system. The mean vertical fluid velocity $\langle u_z \rangle$ (with angular brackets here denoting the time and volume average over the fluid phase) calculated in this system is readily converted to the mean particle settling velocity in a sedimentation setup in which the mean overall volumetric flux of the mixture vanishes (see, e.g., [11]). Upon effecting this change of axes we can compare our results with numerous others available in the literature. We have done so in our earlier paper [19], finding good agreement with the Richardson-Zaki correlation as modified in later work (see, e.g., Refs. [9–11]). The reader is referred to that paper for details.

Due to numerical error and random fluctuations, the mean particle velocity does not remain zero even if it is so initialized. To avoid the drift that would unavoidably accumulate over time due to these factors, the applied pressure gradient is adjusted by means of a proportional-integral-derivative controller (PID) ensuring that the mean particle acceleration vanishes at each time step. The adjustments are very small and they take place at a very high frequency incommensurate with any of the other timescales exhibited by the numerical results. A careful analysis has convinced us that no significant artifacts are introduced by this procedure.

In principle, the physically relevant velocity to be used in the scaling of the numerical results is the mean fluid-particle relative velocity which, however, is itself a result of the calculations. For convenience we will therefore use a reference fluid-particle relative velocity \tilde{u} defined by

$$\frac{\tilde{u}}{w_t} = (1 - \phi)^{n-1}, \quad (3)$$

in which n is the Richardson-Zaki exponent for which Garside and Al-Dibouni [8] give the relation

$$\frac{5.1 - n}{n - 2.7} = 0.1 \text{Re}_t^{0.9}. \quad (4)$$

The reference velocity (3) has the advantage of being easy to calculate from a knowledge of w_t for which reliable correlations are available in the literature (see, e.g., [24]). The values of n used in the

TABLE III. Calculated vertical mean fluid velocity $\langle u_z \rangle$ normalized by the reference velocity (3) and dimensionless particle characteristic time defined in (5) for the present simulations; n is the exponent from (4).

ρ_p/ρ_f	$\phi(\%)$	$\langle u_z \rangle/\tilde{u}$	$\tau_p \tilde{u}/d$	ρ_p/ρ_f	$\phi(\%)$	$\langle u_z \rangle/\tilde{u}$	$\tau_p \tilde{u}/d$
2.0	8.7	0.871	1.515	4.0	8.7	0.852	4.646
$n = 3.305$	17.5	0.881	1.315	$n = 3.052$	17.5	0.845	4.198
	26.2	0.899	1.112		26.2	0.866	3.672
	34.9	0.884	0.926		34.9	0.882	3.155
3.3	8.7	0.860	3.475	5.0	8.7	0.857	6.375
$n = 3.102$	17.5	0.850	3.125	$n = 3.003$	17.5	0.851	5.796
	26.2	0.871	2.713		26.2	0.868	5.118
	34.9	0.874	2.325		34.9	0.873	4.460

present paper to calculate (3) are shown in Table III; they have been discussed and compared with other work in Ref. [19].

The relation between the calculated vertical mean fluid-particle velocity and the reference velocity (3) is shown in Table III, which confirms the close quantitative relationship of the two quantities. The difference of $\langle u_z \rangle/\tilde{u}$ from 1 shows the need for the modification of the Richardson-Zaki correlation by the insertion of a prefactor as mentioned before. Table III also includes the normalized characteristic particle relaxation time τ_p defined by

$$\tau_p = \frac{d^2}{18\nu} \frac{\rho_p}{\rho_f} \left[1 + 0.15 \left(\frac{d\langle u_z \rangle}{\nu} \right)^{0.687} \right]^{-1}. \quad (5)$$

The mean particle-fluid relative velocity can be readily found from the data in the table as $\langle u_z \rangle/(1 - \phi)$ (see, e.g., [11]).

A. Clustering

The quantity

$$\frac{\langle [w'_i(t)]^2 \rangle}{\langle u_z^2 \rangle} = \frac{\langle [w_i(t) - \langle w_i \rangle]^2 \rangle}{\langle u_z^2 \rangle} \quad (6)$$

represents the instantaneous fluctuation of the square of the particle velocity in the vertical ($i = z$) and horizontal ($i = x, y$) directions. The mean values of this quantity in the two directions are represented by the horizontal lines in Figs. 1(a) and 1(b). The upper lines in these two figures show examples of the time dependence of the vertical component of this quantity for a low-concentration [Fig. 1(a)] and a high-concentration [Fig. 1(b)] case, $\phi = 8.7\%$ and $\phi = 34.9\%$, respectively, with $\rho_p/\rho_f = 3.3$. The lower lines represent the analogous horizontal velocity fluctuations. While the latter exhibit small statistical fluctuations around their mean value, a striking feature of the squared vertical particle velocity fluctuations is the presence of long-lived prominent peaks above and minima below the mean values. The intervals of time during which the fluctuation differs by $\pm 10\%$ from the mean are highlighted in the figures. For both volume fractions the peaks can be as large as 35% above the mean value and are interspersed by smaller-amplitude fluctuations. For the higher-concentration case the peaks are more frequent and have a shorter duration. In both cases the lifetime of the peaks is longer than the particle integral timescale defined in (15) and shown later in Fig. 11. In spite of their magnitude, as shown in Fig. 9 of the Supplemental Material, these velocity fluctuations are smaller than those reported in the literature for Stokes flow.

Since the particle velocity averaged over all the particles vanishes, the upper lines in the figure also represent the mean square of the vertical particle velocity fluctuations. It would therefore be difficult to explain the presence of the long-lived high peaks other than by the formation of relatively

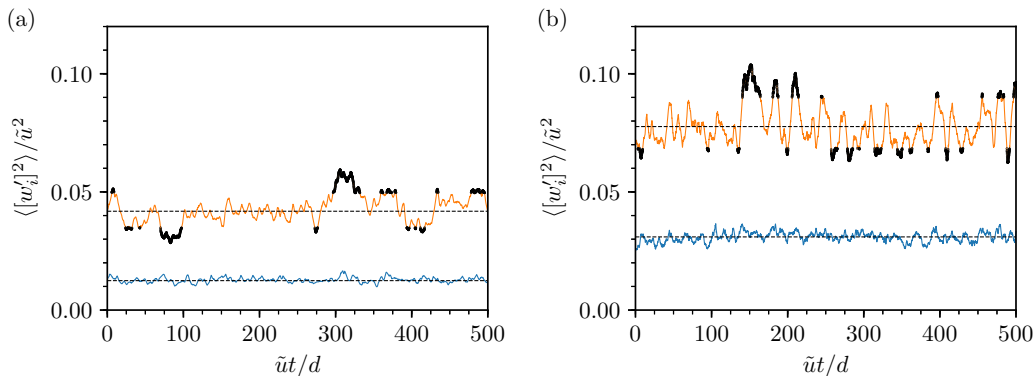


FIG. 1. Two examples of the time dependence of the instantaneous fluctuations of the square of the particle velocity in the vertical (orange upper lines) and horizontal directions with respect to the time-mean values indicated by the horizontal lines for (a) $\phi = 8.7\%$ and (b) $\phi = 34.9\%$, both with $\rho_p/\rho_f = 3.3$. The intervals of time during which the vertical velocity fluctuation differs by $\pm 10\%$ from the mean are highlighted. The time history shown is a fraction of the total length of the simulation. The reference velocity \bar{u} is defined in (3).

long-lived particle clusters involving enough particles to leave a visible signature on the mean settling velocity. The total drag on the particles forming the cluster would be less than if the particles were well separated, and this would increase the relative particle-fluid velocity causing the peaks. During the periods of smaller-than-average velocities, particles may be relatively well separated and “fall” close to their terminal velocity relative to the fluid, which would be exactly zero in a completely homogeneous system. The shorter lifetime of clusters with increasing particle volume fraction demonstrated in Fig. 1 can be explained by the increasing importance of collisions or, more generally, particle-particle interactions, which would tend to disrupt close particle arrangements.

The presence of clusters is visually evident in the movies available as Supplemental Material [18] for this paper. Nicolai *et al.* [25] observed the existence of clusters in their experiments, as did Ladd [26] in his simulations, with both studies in the low-Reynolds-number regime. The more recent study by Uhlmann and Doychev [27] at two values of the Galilei number $Ga = 121$ and 178 also showed the presence of clusters at $Ga = 178$, but not as clearly for $Ga = 121$. These authors explained their results on the basis of known features of single-particle settling wakes, which are certainly important at the very dilute conditions that they considered, $\phi = 0.5\%$. These considerations, however, are probably not very relevant for the present range of concentrations and, besides, the study at two values of Ga did not permit them to establish whether the clustering that they observed has a gradual or an abrupt onset.

Uhlmann and Doychev [27] established their results on clustering by means of an analysis of the Voronoi tessellation of their particle centers. The results of a similar analysis for the cases of Fig. 1 are shown in Fig. 2 [28]; the lines marked with circles and squares (blue and orange, respectively) have been obtained by averaging the Voronoi probability distribution function (PDF) over the time intervals of greater- or lower-than-average velocity marked in black in Fig. 1. For the lower volume fraction [Fig. 1(a)] one can detect a slight bias toward smaller volumes, but for the higher volume fraction [Fig. 1(b)] the two lines are essentially superposed.

An alternative to the Voronoi analysis is the following. Let $n(r)$ be the average number density of particles with center in spherical shells of different radii r centered on each particle (referred to as a test particle) during the periods of time highlighted in Fig. 1; the test particle is included in the count. Figure 3 shows the PDF of this number divided by the mean number density $n(r)/\langle n \rangle$ for $r/a = 2.25, 2.50, 3,$ and 3.50 ; the vertical dashed line shows the average number density over the entire computational domain. The smaller the radius, the larger the fluctuations. The solid and dashed lines are the average number densities of particles during the high- and low-velocity intervals, respectively. For the low-concentration case $\phi = 8.7\%$ [Fig. 3(a)] there is a significant

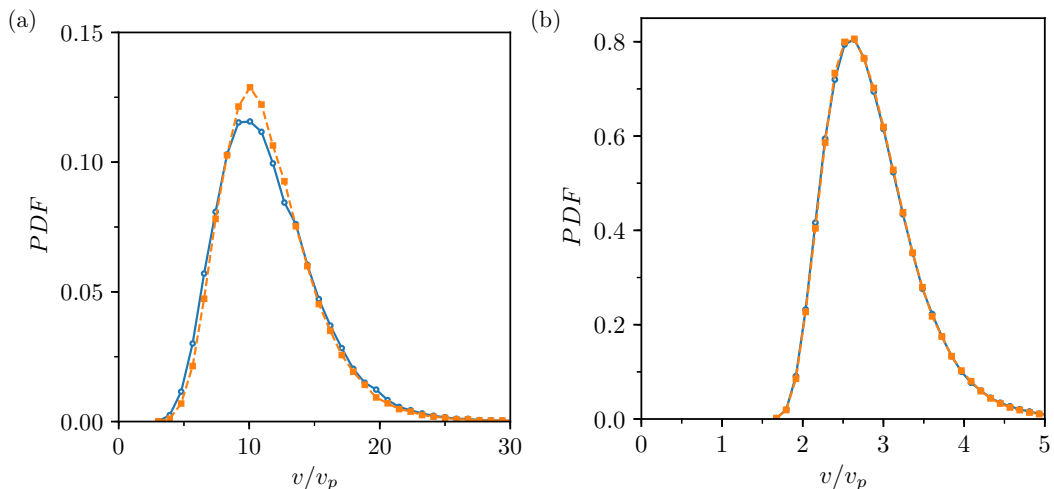


FIG. 2. Probability density function of Voronoi volumes normalized by the particle volume $v_p = \frac{\pi}{6}d^3$ for the two cases of Fig. 1, namely, (a) $\phi = 8.7\%$ and (b) $\phi = 34.9\%$, both with $\rho_p/\rho_f = 3.3$. The blue lines marked with circles are the average for the periods of greater-than-average velocity in Fig. 1, while the orange lines marked with squares are the average for the periods of smaller-than-average velocity. In (b) the two lines are essentially superposed while in (a) a somewhat larger probability for smaller values of the Voronoi volumes is visible for the greater-than-average velocity periods.

probability of finding a normalized number density during the peak events larger than that during the periods of low values of $\langle w_z^2 \rangle$. In reading these figures it should be noted that the tick marks are separated by two orders of magnitude and the curves, in the region of interest, are nearly vertical. For the higher volume fraction [Fig. 3(b)] differences become legible only for the largest radius $r/a = 3.50$ (red). Since, in this case, the average particle number density is larger, revealing the concentration anomaly requires counting a larger number of particles and therefore a larger r . Additional results of this type for the other cases simulated are presented in the Supplemental Material. Interestingly, the effect appears to be present not only for $n(r) > \langle n \rangle$, but also for $n(r) < \langle n \rangle$, in which the particle number is smaller. Since, for r fixed, there can be many more

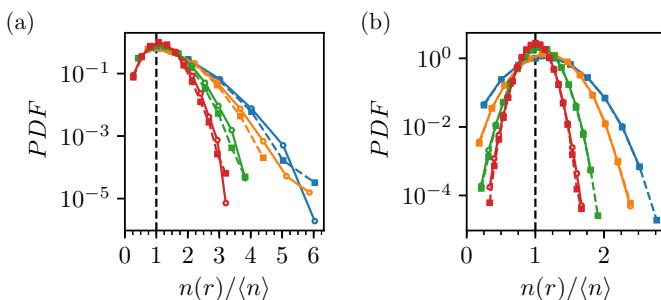


FIG. 3. Plot of the PDF of $n(r)/\langle n \rangle$, with $n(r)$ the average number density of particles with center in spherical shells of different radii r centered on each particle during the periods of time highlighted in Fig. 1, $\langle n \rangle$ the mean number density over the computational domain, for $r/a = 2.25$ (blue), 2.50 (orange), 3 (green), and 3.50 (red), and the same conditions as in Figs. 1 and 2. The solid and dashed lines are the values of $n(r)/\langle n \rangle$ during the high- and low-velocity intervals, respectively. (a) For the low-concentration case note the higher probability of larger values of $n(r)/\langle n \rangle$ during the higher-velocity periods highlighted in Fig. 1. (b) For the denser case, this effect is only apparent for $r = 3.5a$ (red) and it is also present for $n(r) < \langle n \rangle$.

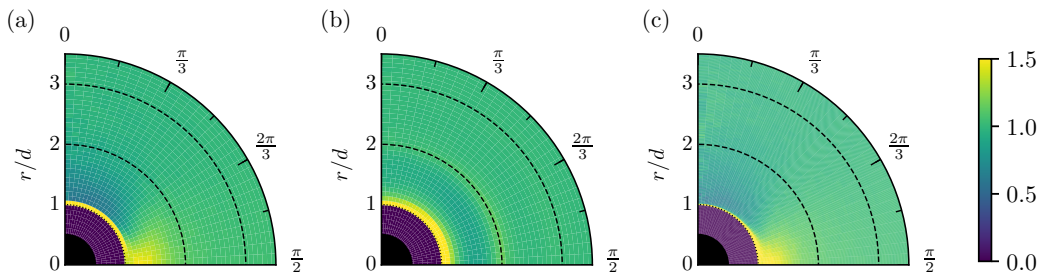


FIG. 4. Pair distribution function $g(r, \theta)$ for (a) $\phi = 8.7\%$ and (b) $\phi = 34.9\%$ with $\rho_p/\rho_f = 2$ ($\text{Re}_t = 43.27$) and for (c) $\phi = 8.7\%$ with $\rho_p/\rho_f = 5$ ($\text{Re}_t = 110.8$).

particles near the test particle in the dense as compared with the dilute case, there is a significantly larger probability to encounter spherical shells with $n(r) < \langle n \rangle$. These results support the conjecture that the peak periods of $\langle w_z^2 \rangle$ correspond to the formation of denser particle clusters which extend at least as far as $r = 3.5a$. This clustering effect appears to be weaker at the higher volume fractions, for which the Voronoi analysis does not suggest any clustering while the alternative one gives a weak indication of its presence. An examination of the probability density function of w_z (not shown) reveals that high-velocity events with $w_z > 0$ and $w_z < 0$ occur in approximately the same number, although the frequency of the events with $w_z > 0$ tends to increase slightly with the volume fraction.

B. Two-particle distribution function

Several investigators have studied the two-particle distribution function $g(r, \theta)$ in systems of the type investigated here. Yin and Koch [11] and Hamid *et al.* [14] considered single-particle Reynolds numbers up to 20 and 10, respectively, while the Reynolds-number range considered in [13] extends up to 50; all these authors considered volume fractions comparable to ours.

For low concentrations, all these studies agree in reporting an anisotropic distribution with more particles near the test particle in the horizontal direction, $\theta \sim \pi/2$, and fewer particles in the vertical direction, $\theta \sim 0$. Yin and Koch [11] find the greatest anisotropy for $\phi = 1\%$ and $\text{Re}_t = 10$, a regime in which the mixture behavior is dominated by anisotropic wake interactions. As the volume fraction increases, the anisotropy decreases. Increased inertia from $\text{Re}_t = 1$ to 10 enhances the anisotropy [11, 14]. The origin of this preferential arrangement, which has theoretically been known for a long time (see, e.g., [29, 30]) and verified experimentally [31], lies essentially in a Bernoulli effect as the flow blockage offered by two neighboring particles increases the velocity of the fluid between them and lowers the pressure.

The Reynolds-number range in the present work goes up to 110, but the results found by previous investigators for smaller inertia are essentially confirmed. Figure 4 shows the two-particle distribution function for $\phi = 8.7\%$ and 34.9% with $\rho_p/\rho_f = 2$ ($\text{Re}_t = 43.27$), as well as $\phi = 8.7\%$ with $\rho_p/\rho_f = 5$ ($\text{Re}_t = 110.8$); additional results of this type are shown in the Supplemental Material [18]. A comparison between Figs. 4(a) and 4(b) (constant Re_t , increasing ϕ) shows the fading of the anisotropy with increasing concentration. A comparison between Figs. 4(a) and 4(c) shows the enhanced particle number in the horizontal direction and closer to the test particle caused by the increased inertia in the latter one. A different view of the same information is provided in Fig. 5, where the lines show three angular averages of $g(r, \theta)$. The solid lines are the average over the entire range $0 \leq \theta \leq \pi/2$, the dashed lines are the average over a vertical sector $0 \leq \theta \leq \pi/12$, and the dotted lines are the average over a horizontal sector $5\pi/12 \leq \theta \leq \pi/2$. A comparison of Figs. 5(a) and 5(b) ($\phi = 8.7\%$ and 34.9% , $\text{Re}_t = 43.27$), shows that the anisotropy strongly decreases as the concentration increases, although it is not completely removed. The peaks around $r/2a = 2$ indicate the gradual buildup of a “cage” of particles around the test particle, with a slightly stronger effect in the horizontal direction.

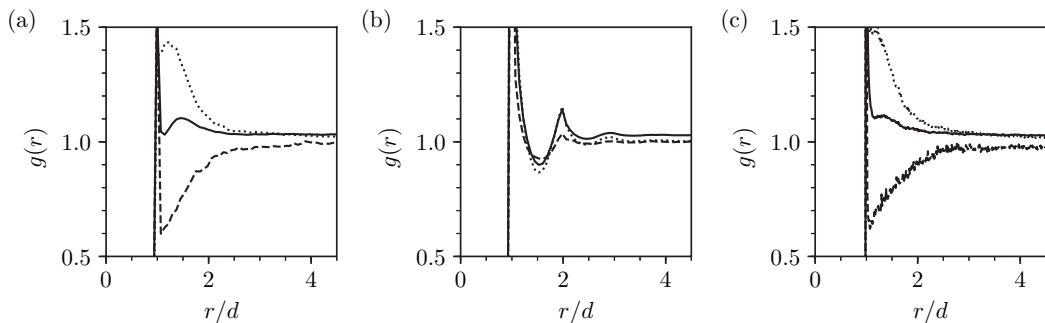


FIG. 5. Angular averages of the pair distribution functions shown in Fig. 4. The solid lines are the average over the entire range $0 \leq \theta \leq \pi/2$; the dashed lines are the average over a vertical sector $0 \leq \theta \leq \pi/12$ and the dotted lines over a horizontal sector $5\pi/12 \leq \theta \leq \pi/2$.

For the largest Reynolds number [Fig. 5(c)] the peak in the horizontal direction is higher and it moves closer to the test particle. The average in the vertical sector extends further out from the test particle and is slightly decreased. A plausible explanation of these results is that, at higher Re_t , the vertical orientation of particle pairs is less stable as the couple that causes the broad-side rotation is stronger and the fluid dynamic force that tends to separate horizontal pairs is less effective due to the particle inertia.

C. Particle collisions

A specific phenomenon caused by larger inertia, particularly at moderate to large volume fractions, is an increased frequency of particle collisions. As described in [17], the collision algorithm used in the simulations embodies a nonlinear Hertzian contact model which is activated whenever the distance between two particle centers becomes equal to a diameter. This model is complemented by a lubrication interaction when the distance between the particle surfaces is less than a radius. Figure 6 shows our results for the volume fraction dependence of the normalized collisional frequency f_* ,

$$f_* = f_c d \left(\frac{1}{3} \langle \mathbf{w} \cdot \mathbf{w} \rangle \right)^{-1/2}, \quad (7)$$

with f_c the computed value and the angular brackets denoting the particle average as before. The results shown are the average number of actual Hertzian contacts per particle per unit time. Normalization by the particle number is useful in that it admits proper accounting of multiparticle collisions. The dashed line is the Enskog collision frequency for elastic hard spheres (see, e.g., [32,33])

$$f_E = 4g_2(\phi)d^2n\sqrt{\frac{\pi}{3}\langle \mathbf{w} \cdot \mathbf{w} \rangle}, \quad (8)$$

normalized in the same way; here $g_2(\phi)$ is the angle-averaged two-particle distribution function at contact, approximated by the Carnahan-Starling formula

$$g_2(\phi) = \frac{1}{2} \frac{2 - \phi}{(1 - \phi)^3}. \quad (9)$$

Given the presence of hydrodynamic resistance, kinetic theory overpredicts the computed collisional frequency, although it provides a good account of the volume fraction dependence except for the lightest particles, which are most affected by the fluid. The collisional frequency increases with the particle mass, as expected from the fact that, with larger inertia, hydrodynamic forces become less and less able to prevent a close approach. The division of the collisional frequency by $\sqrt{\rho_p/\rho_f}$ produces an approximate collapse of the results as shown in Fig. 6(b). This result might reflect a role

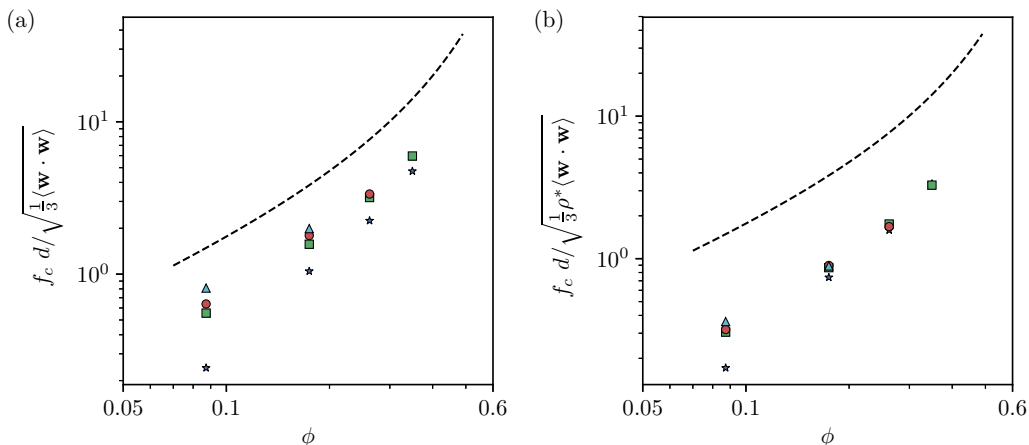


FIG. 6. Particle collision frequency normalized as in (7) vs volume fraction for the systems simulated in this study. The symbols denote the particle-to-fluid density ratios $\rho^* = \rho_p/\rho_f = 2$ (asterisks), 3.3 (squares), 4 (circles), and 5 (triangles). The dashed lines are the predictions from the theory of granular flows.

of the added mass in determining the relevant mean particle kinetic energy $\langle \mathbf{w} \cdot \mathbf{w} \rangle$ for the purposes of scaling some aspects of the system dynamics; a similar collapse is found below for the particle diffusivity.

D. Particle diffusion coefficient

The connection between the particle velocity correlation tensor $\langle w_i(t + \tau)w_j(t) \rangle$ and the particle diffusivity D_p is well known,

$$D_p^{(ij)} = \lim_{t \rightarrow \infty} \frac{1}{2t} \langle r_i(t)r_j(t) \rangle = \lim_{t \rightarrow \infty} \int_0^t \langle w_i(\tau)w_j(0) \rangle d\tau, \quad (10)$$

in which $r_i(t) = x_i(t) - x_i(0) - \int_0^t \langle w_i(\tau) \rangle d\tau$ is the displacement of the test particle from the initial position corrected for the mean displacement of all the particles. While in principle $D_p^{(ij)}$ is a tensorial quantity, we find that the off-diagonal components are very small so that we limit ourselves to presenting results for the diffusivity in the vertical and in the horizontal directions D_p^z and D_p^\perp , respectively, the latter calculated in the horizontal plane.

The time dependence of $\langle r_z^2(t) \rangle / 2t$ and $\langle r_\perp^2(t) \rangle / 2t$ is shown in Fig. 7(a), where the asymptotic approach to a constant for both the vertical and horizontal directions is evident. Figure 7(b) shows instead $\langle r_z^2(t) \rangle / t^2$ and $\langle r_\perp^2(t) \rangle / t^2$. The constant values of these quantities for short times indicate the prevalence of the so-called ballistic regime, during which the particle velocity maintains a correlation with itself.

The two sides of (10) provide two alternative ways to calculate the particle diffusivity, one from the mean-square displacement, the other from the integral of the velocity correlation. The results for D_p^z and D_p^\perp calculated from the mean-square displacement as shown in Fig. 7(a) are shown in Figs. 8(a) and 8(b), in which the dashed line is the prediction from the kinetic theory of granular gases (see, e.g., [33]), corrected for the factor of 3 used in the definition of the diffusion coefficient in that theory:

$$D_E = \frac{9}{8} \frac{1}{d^2 g_2(\phi) n} \sqrt{\frac{1}{3} \langle \mathbf{w} \cdot \mathbf{w} \rangle}. \quad (11)$$

The results are made dimensionless by division by $\sqrt{\frac{1}{3} \langle \mathbf{w} \cdot \mathbf{w} \rangle}$. The computed and kinetic theory results are comparable in magnitude, but there are significant differences in their concentration

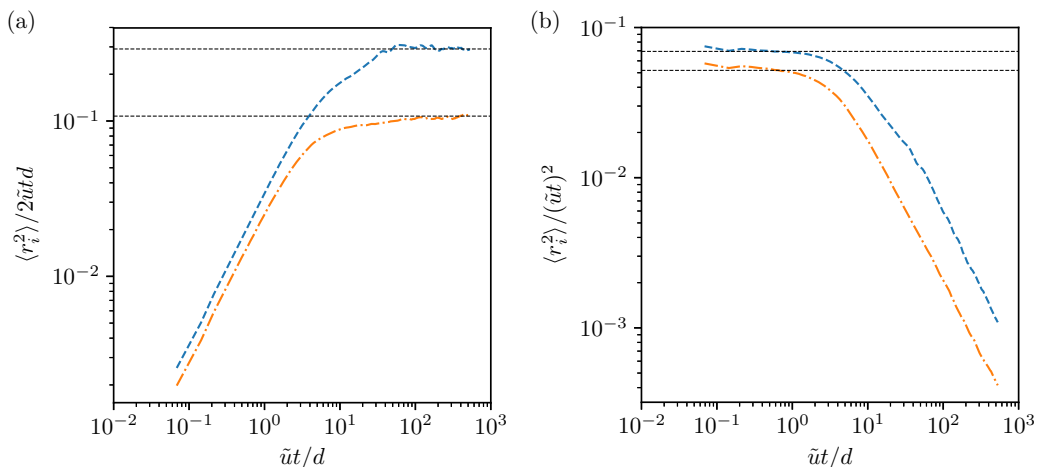


FIG. 7. Examples of the time dependence of the mean-square particle displacement in the vertical $\langle r_z^2(t) \rangle / 2\tilde{u}td$ (upper lines) and horizontal $\langle r_\perp^2(t) \rangle / 2\tilde{u}td$ directions. In (b) the displacement is normalized by $\tilde{u}^2 t^2$. The horizontal lines are the long-time and short-time mean values.

dependence. In the vertical direction, for $\phi = 8.7\%$, kinetic theory overpredicts the diffusivity, probably as a result of the hydrodynamic force on the particles that hinders their random motion. However, the trend reverses with increasing ϕ , for which kinetic theory predicts a much stronger decrease than that found in the simulations. A likely explanation is that the flowing fluid enhances the mobility of the test particle by breaking up the cages formed by the surrounding particles, thus favoring its escape. While the flowing fluid enhances the vertical particle displacements, it has a much smaller effect in the horizontal direction. Thus, the horizontal diffusivity is lower than the kinetic theory prediction at low volume fractions due to hydrodynamic resistance, while it is found to follow the kinetic theory prediction at higher concentration for which the absence of a mean flow does not enhance particle mobilities. This explanation is in accordance with the buildup of the cage structure mentioned before and with the radial distribution function mentioned at the end of Sec. III B. Interestingly, as shown in the Supplemental Material [18], a division of both D_p^z and D_p^\perp by $\sqrt{\rho_p/\rho_f}$ provides an excellent collapse of both diffusivities similarly to what was found for the collisional frequency. Figure 8(c) is the ratio D_p^z/D_p^\perp ; one observes a marked anisotropy with a minimum around $\phi \simeq 26.2\%$.

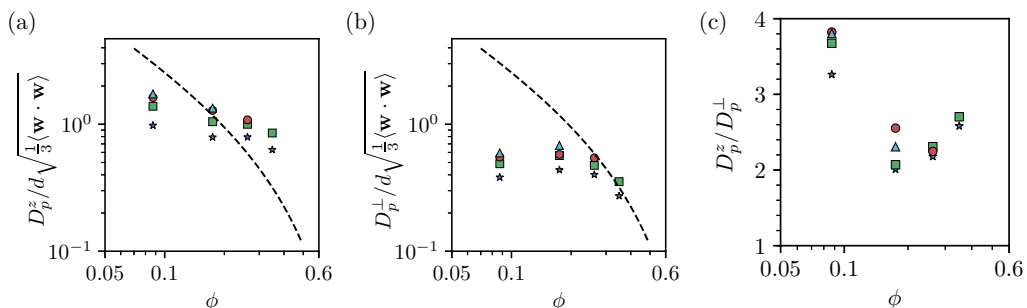


FIG. 8. Particle diffusivities in the (a) vertical and (b) horizontal directions normalized as in (11) and (c) the ratio of the two diffusivities, illustrating the marked anisotropy of the diffusion process in the system investigated. The dashed lines are the predictions from the theory of granular flows (11). The symbols denote the different particle-to-fluid density ratios $\rho_p/\rho_f = 2$ (asterisks), 3.3 (squares), 4 (circles), and 5 (triangles).

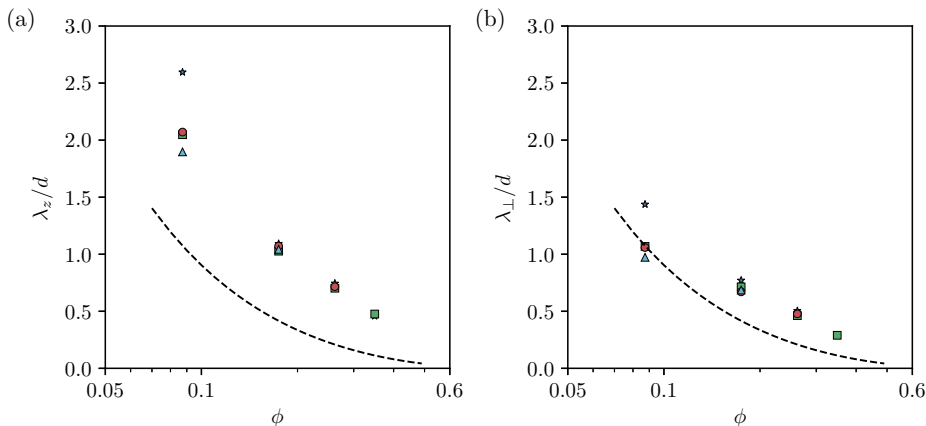


FIG. 9. Normalized particle mean free path defined in (12) in the (a) vertical and (b) horizontal directions. The dashed line is the kinetic theory prediction (13). The symbols denote the different particle-to-fluid density ratios $\rho_p/\rho_f = 2$ (asterisks), 3.3 (squares), 4 (circles), and 5 (triangles).

In the Stokes regime the diffusivity is predicted to scale proportionally to the product of the particle diameter and the mean particle-fluid velocity [34,35]. We have tried to normalize our calculated results for the diffusivity by d/\bar{u} (see Fig. 13 below) and by d/w_t (Fig. 5 of the Supplemental Material), but we found that these scalings do not collapse them any better than the scaling used in plotting Fig. 8.

Following the approach of kinetic theory, we can obtain an estimate of the particle mean free path λ as

$$\frac{\lambda_{ii}}{d} = \sqrt{\frac{D_p^{ii}}{f_c d^2}}. \quad (12)$$

The kinetic theory prediction for this quantity is

$$\frac{\lambda_E}{d} = \frac{1}{6\sqrt{2}\phi g_2(\phi)}. \quad (13)$$

Figure 9 compares these two quantities. In the vertical direction, our calculated mean free path is longer than the kinetic theory prediction, in agreement with the enhanced mobility previously demonstrated by the results for D_p^z . In addition, the flow caused by a particle tends to displace the particles toward which it moves, a process that cannot happen in a granular gas without interstitial fluid. This effect is analogous to that of a repulsive inter-particle force in kinetic theory, which is also known to increase the diffusivity (see, e.g., [36]). In the horizontal direction kinetic theory underpredicts the mean free path as well, but by a significantly smaller margin. Again we see here the effect of the absence of a mean horizontal fluid velocity resisted by a force comparable to gravity.

We now turn to the second way to estimate the diffusivity, namely, by integrating the normalized velocity correlation

$$R_{ii} = \frac{\langle w_i(t)w_i(0) \rangle}{\langle w_i^2 \rangle}. \quad (14)$$

It may be noted that the denominator is the same quantity shown by the horizontal lines in Fig. 1. Figure 10 shows two examples of the dependence of R_{ii} on time for $\rho_p/\rho_f = 3.3$ and $\phi = 8.7\%$ and 34.9% with two different normalizations, the particle relaxation time on the lower horizontal axis and the particle settling time on the upper one. Comparison of these two scales reveals that the velocity remains correlated for a time during which particles fall by about three diameters. As found

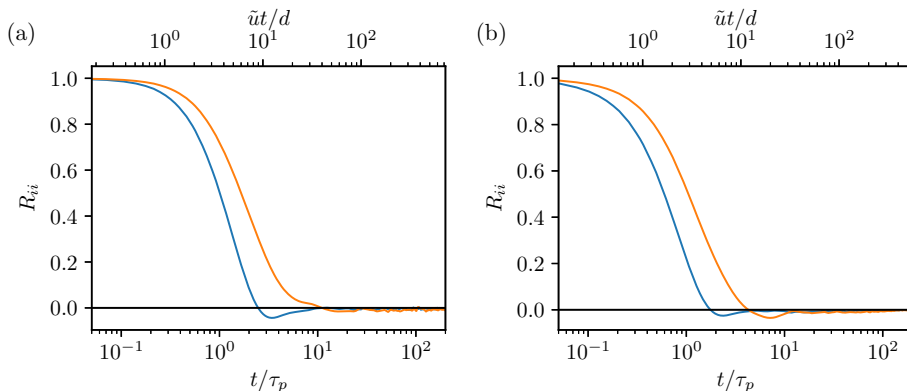


FIG. 10. Two examples of the velocity autocorrelation (14) for (a) $\phi = 8.7\%$ and (b) $\phi = 34.9\%$, both for $\rho_p/\rho_f = 3.3$. The orange upper and blue lower lines are for the horizontal and vertical velocities, respectively. On the lower horizontal axis time is normalized by the particle relaxation time τ_p defined in (5). On the upper axis time is normalized by the particle settling timescale $\bar{u}t/d$.

by several earlier investigators [12,14,25], the velocity decorrelates much faster in the horizontal direction than in the vertical. The correlation lasts longer at low volume fraction due to the weaker particle-particle interactions caused by the larger mean separation.

To examine the importance of direct collisions on the correlation we can examine the integral timescale defined by

$$\mathcal{T}_{ii} = \lim_{t \rightarrow \infty} \int_0^t \frac{\langle w_i(\tau)w_i(0) \rangle}{\langle w_i^2 \rangle} d\tau, \quad (15)$$

the average of which is shown in Fig. 11 normalized by d/\bar{u} . This timescale shows a strong decrease with increasing ϕ . If direct collisions were the major factor affecting the velocity correlations, one would expect that the product $\mathcal{T}_{ii}f_c$ would be approximately constant. This, however, is not the case as shown in Fig. 12, where this product is found to undergo a marked increase with ϕ , primarily due to the increase of the collisional frequency. This result indicates that direct collisions are mostly

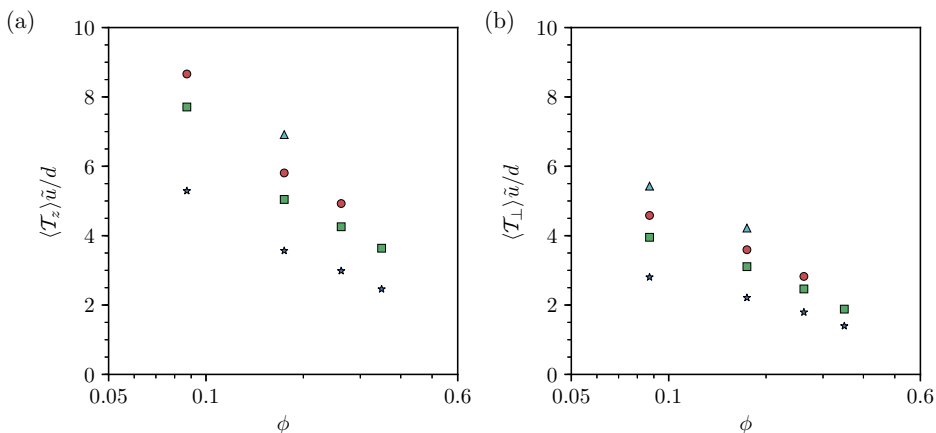


FIG. 11. Normalized integral timescale defined in (15) in the (a) vertical and (b) horizontal directions. The symbols denote the different particle-to-fluid density ratios $\rho_p/\rho_f = 2$ (asterisks), 3.3 (squares), 4 (circles), and 5 (triangles).

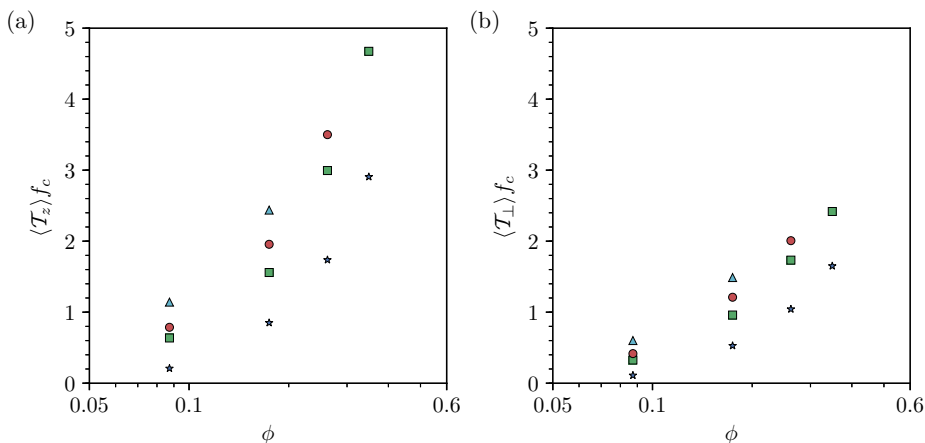


FIG. 12. Integral timescale defined in (15) in the (a) vertical and (b) horizontal directions normalized by the collision frequency.

weak, as already remarked in Sec. II. The conclusion that must be drawn is that the most significant agents causing the decorrelation of a particle velocity are the flow fields produced by the particles that it encounters rather than direct contacts as in a granular gas.

The result for the particle diffusivity calculated from the velocity correlation integral (open symbols) is compared with that calculated with the mean-square displacement shown earlier (closed symbols) in Fig. 13. Here, unlike Fig. 8, we normalize D_p by $\tilde{u}d$ to bring out the presence of a maximum around $\phi \sim 10\text{--}15\%$, which was also found, e.g., in [14]. The effect of this normalization is due to the rapid decrease of the mean fluid-particle relative velocity with particle concentration, as represented by \tilde{u} , which is faster than the decrease of $\sqrt{\langle \mathbf{w} \cdot \mathbf{w} \rangle}$. This second normalization, however, appears to be less justified by the physics of the particle diffusion, which is directly dependent on the particle velocity fluctuations, incorporated in the earlier normalization by the use of $\sqrt{\langle \mathbf{w} \cdot \mathbf{w} \rangle}$.

The two ways to calculate D_p have an average difference of 5%. In view of the difficulty of accurately estimating the velocity correlation and its integral, reliance on the mean-square displacement method is probably justified.

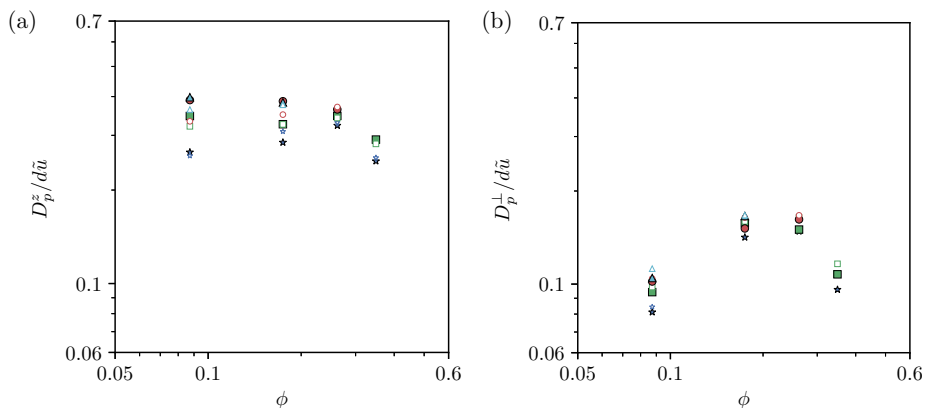


FIG. 13. Open symbols show the particle diffusivities in the (a) vertical and (b) horizontal directions as obtained from integration of the velocity correlation normalized by $d\tilde{u}$; the closed symbols are the same as in Fig. 8 with this different normalization. The symbols denote the different particle-to-fluid density ratios $\rho_p / \rho_f = 2$ (asterisks), 3.3 (squares), 4 (circles), and 5 (triangles).

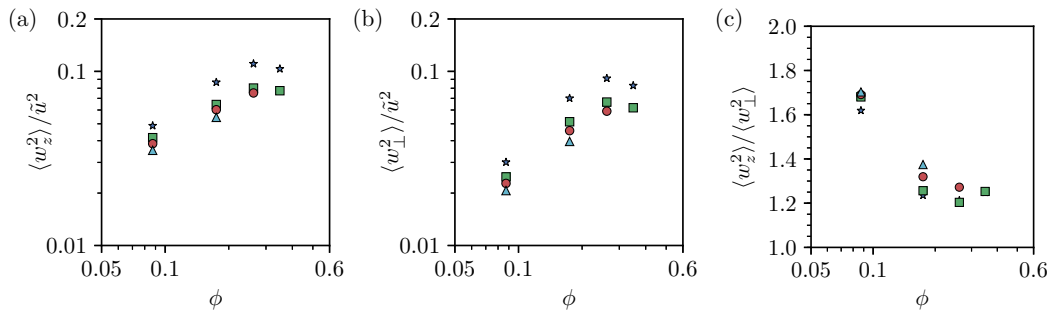


FIG. 14. Particle velocity fluctuations in the (a) vertical and (b) horizontal directions; (c) the ratio of the two, which indicates a marked anisotropy. The symbols denote the different particle-to-fluid density ratios $\rho_p/\rho_f = 2$ (asterisks), 3.3 (squares), 4 (circles), and 5 (triangles).

E. Velocity fluctuations

Velocity fluctuations in sedimenting suspensions have been investigated by many authors motivated by the predicted divergence with container size at low Reynolds numbers. The current understanding of this matter is summarized in the review in [16]. Since our domain size is fixed, we cannot comment on this aspect.

Our results for the particle velocity fluctuations normalized by the particle terminal velocity w_t (not shown) confirm those presented in [14] in their common Reynolds-number range. We find a peak at our second lowest volume fraction ($\phi = 17.5\%$) and a decrease thereafter. Figure 14 shows the present results normalized by \bar{u} rather than w_t . With this normalization the fluctuations increase with ϕ and appear to saturate at our largest volume fraction $\phi = 34.9\%$. The different trends obtained with the two normalizations depend on the fact that, while \bar{u} decreases with concentration, w_t is independent of the particle concentration. At the larger Reynolds numbers they studied, $\text{Re}_t = 20$, Ref. [37] found a very slow decay of $\langle w_z^2 \rangle / w_t^2$. We find similar results in our higher-Reynolds-number range for all the volume fractions we simulated.

Figure 14(c) is the ratio of the vertical and horizontal velocity fluctuations. There is a marked anisotropy with a minimum around $\phi = 26.2\%$ which, not coincidentally, occurs at the same volume fraction where the anisotropy of the diffusivities is also a minimum.

In Fig. 9 of the Supplemental Material, the velocity fluctuations encountered in this study are compared with those available in the literature at Reynolds numbers of order 10^{-4} – 10^{-3} summarized in Fig. 4 of Ref. [16]. Qualitatively, the fluctuations that we calculate tend to be significantly smaller (by about a factor of 2) than those found at small Reynolds numbers. A plausible explanation of this difference is that, at small Reynolds number, the region of fluid affected by a particle is not mostly limited to the wake, as at finite Reynolds number, but extends much farther out thus affecting many more particles.

IV. TETRADS

Some interesting information on the behavior of the system under consideration can be obtained by a study of the time evolution of the shape and orientation of groups of four particles: particle tetrads. This study enables us to probe the small-scale dynamics of the particulate phase beyond the one- and two-particle information considered up to this point. Studies of this type have been carried out, e.g., in polymer science (see, e.g., [38,39]), the theory of random walks (see, e.g., [40]), single-phase turbulence (see, e.g., [41–44]), and other areas (see, e.g., [45]).

A. Tetrad geometry

Several different ways of investigating tetrad geometry have been proposed (see, e.g., [44]). We use an approach common in the polymer literature [38,40] in view of its intuitive appeal.

At each instant of time, we define a coarse-grained velocity gradient tensor \mathbf{M}_{ji} around the instantaneous center of each tetrad by minimizing the quantity [44]

$$K = \sum_{n=1}^4 \sum_{i=1}^3 \left[(w_i^n - \bar{w}_i) - \sum_{j=1}^3 (x_j^n - \bar{x}_j) \mathbf{M}_{ji} \right]^2, \quad (16)$$

in which x_i^n and w_i^n represent the i th component of position and velocity of the n th particle in the tetrad and

$$\bar{x}_i = \frac{1}{4} \sum_{n=1}^4 x_i^n, \quad \bar{w}_i = \frac{1}{4} \sum_{n=1}^4 w_i^n \quad (17)$$

are the position and velocity of the center of the tetrad. The velocity gradient tensor \mathbf{M}_{ji} that minimizes K is the solution of the linear system

$$\sum_{k=1}^3 \mathbf{G}_{ik} \mathbf{M}_{kj} = \mathbf{W}_{ij}, \quad (18)$$

in which \mathbf{G}_{ik} is the shape (or gyration) tensor [38,39,46]

$$\mathbf{G}_{ij} = \frac{1}{4} \sum_{n=1}^4 (x_i^n - \bar{x}_i)(x_j^n - \bar{x}_j) \quad (19)$$

and

$$\mathbf{W}_{ij} = \frac{1}{4} \sum_{n=1}^4 (x_i^n - \bar{x}_i)(w_j^n - \bar{w}_j). \quad (20)$$

The eigenvectors of the shape tensor

$$\mathbf{G} \mathbf{v}_k = \lambda_k \mathbf{v}_k, \quad (21)$$

with λ_k the respective eigenvalues, identify the principal axes of the tetrad orientation. For an isotropic tetrad, $\lambda_1 = \lambda_2 = \lambda_3$. The normalized eigenvalues

$$I_k = \frac{\lambda_k}{3\bar{\lambda}} \quad (22)$$

are defined in terms of the mean value $\bar{\lambda} = \frac{1}{3}(\lambda_1 + \lambda_2 + \lambda_3)$. The deviation of the normalized eigenvalues from $1/3$ provides a measure of the anisotropy of the shape tensor.

The antisymmetric part of the velocity gradient tensor describes the rotation of the tetrad, while the symmetric part $\mathbf{S}_{ij} = \frac{1}{2}(\mathbf{M}_{ij} + \mathbf{M}_{ji})$, on which we focus, carries information on its deformation. The eigenvectors \mathbf{s}_k of \mathbf{S} are the directions of the principal axes of strain.

The primary measure of the tetrad size is the radius of gyration R_G defined by

$$R_G^2 = \text{Tr}(\mathbf{G}_{ij}) = \lambda_1 + \lambda_2 + \lambda_3 = 3\bar{\lambda}. \quad (23)$$

The shape of the tetrad can be further characterized by two dimensionless parameters: the shape variance Δ , also called relative shape anisotropy, and the shape factor S . The shape variance is defined as

$$\Delta = \frac{3}{2} \frac{\text{Tr}(\hat{\mathbf{G}}_{ij}^2)}{(\text{Tr} \mathbf{G}_{ij})^2}, \quad (24)$$

TABLE IV. Number of tetrads tracked for each case. Entries marked with a centered dot were unavailable.

ϕ	ρ^*	No. of tetrads
0.087	[2, 3.3, 4, 5]	[1376, 2871, 3569, 4332]
0.175	[2,3,3,4,5]	[34327, 52686, 61903, 67910]
0.262	[2, 3.3, 4, ·]	[104230, 174862, 197487, ·]
0.349	[2, 3.3, ·, ·]	[84339, 232426, ·, ·]

where $\text{Tr}(\hat{\mathbf{G}}_{ij}^2) = \sum_{k=1}^3 (\lambda_k - \bar{\lambda})^2$ is proportional to the variance of the eigenvalues of the deviatoric part of \mathbf{G}_{ij} , defined by $\hat{\mathbf{G}}_{ij} = \mathbf{G}_{ij} - \bar{\lambda}\delta_{ij}$. It can be shown that $0 \leq \Delta \leq 1$ [39]. For a spherically symmetric particle arrangement the shape variance vanishes, while it reaches its maximum value 1 when the centers of the four particles fall on a straight line; for a right tetrad with three isosceles triangles $\Delta = 1/9$. The shape factor S is defined by

$$S = 27 \frac{\det(\hat{\mathbf{G}}_{ij})}{[\text{Tr}(\mathbf{G}_{ij})]^3}, \quad (25)$$

where $\det(\hat{\mathbf{G}}_{ij}) = \prod_{k=1}^3 (\lambda_k - \bar{\lambda})$. It can be shown that $-\frac{1}{4} \leq S \leq 2$ [39]. For a prolate particle arrangement $\lambda_1 > \bar{\lambda} > \lambda_2, \lambda_3$ and S is positive, while for an oblate arrangement with $\lambda_1, \lambda_2 > \bar{\lambda} > \lambda_3$, S is negative.

B. Tetrad initialization

At the initial instant of each realization we select four-particle groups with an initial distance between any two particle centers between slightly less than $2a$ (to account for the very small overlap occurring during collisions) and $2.5a$. To ensure a reasonable degree of isotropy in the initial tetrad configuration we only use tetrads with an initial shape variance of $\Delta \leq 0.15$. These choices strike a balance between the number of tetrads sufficient for statistical convergence and the removal of a significant contamination by anisotropic structures.

In view of the triply periodic nature of the simulation, we prefer not to follow the tetrads much beyond the time when the average radius of gyration exceeded $20a$, the shortest dimension of our computational domain. Since this criterion was applied to the average radius of gyration rather than to each individual tetrad, one would expect that the radius of gyration of some tetrads would have exceeded $20a$. However, this is not a serious concern because, as will be seen below, tetrads tend to elongate in the vertical direction, in which the domain size is $60a$ and furthermore one can account for a particle exiting the computational domain simply by adding the width of the domain to the position of its image inside the domain. Since the time to reach $\langle R_G \rangle = 20a$ was shorter than the duration of the simulations, we carved up each simulation into several portions that were used to populate the ensemble over which averages were calculated. The time necessary for a doubling of $\langle R_G \rangle$ was used to define the interval between the starts of successive portions. The number of tetrads tracked in this way for each set of parameters is presented in Table IV.

C. Shape evolution

Results from simulations with different particle densities are represented by different colors: gray for $\rho_p/\rho = 2$, green for $\rho_p/\rho = 3.3$, red for $\rho_p/\rho = 4$, and blue for $\rho_p/\rho = 5$; increasing volume fractions are indicated by increasing color saturation. In the presentation of results used here time is nondimensionalized by d/\bar{u} , and results for the same particle density, but different volume fraction, are essentially superposed so that lines with different hues are barely distinguishable. This collapse shows the effectiveness of the Richardson-Zaki factor $(1 - \phi)^{n-1}$ appearing in the definition (3) of \bar{u} in accounting for the effect of volume fraction. In Fig. 10 of the Supplemental Material we

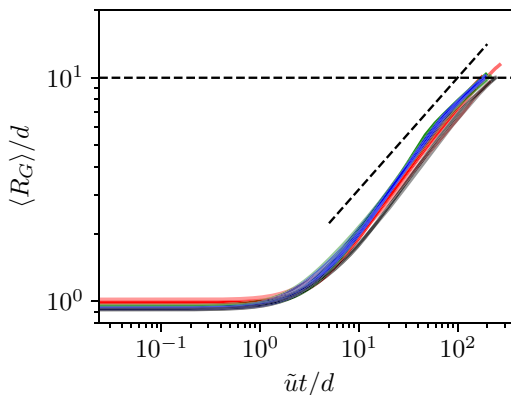


FIG. 15. Time dependence of the normalized mean tetrad radius of gyration defined in (23) for $\rho_p/\rho_f = 2$ (gray), 3.3 (green), 4 (red), and 5 (blue).

nondimensionalize time by the diffusive scale d^2/ν and the effect of volume fraction is more clearly visible.

1. Mean

The radius of gyration averaged over all tetrads is shown as a function of the scaled dimensionless time $\tilde{u}t/d$ in Fig. 15. The horizontal black dashed line identifies the length of the smallest dimension of the computational domain and the other dashed line has a slope 1/2. The timescale d/\tilde{u} does a good job of collapsing all the results not only for different volume fractions, but also very nearly for different particle densities, while it is found that the characteristic time based on the granular temperature does not (not shown).

The tetrads maintain a size close to the initial one for the time required to move by one or a few diameters relative to the fluid, indicating that the constituent particles are still experiencing a similar flow environment and similar hydrodynamics forces. This corresponds to the ballistic regime in Figs. 7(a) and 7(b). At $\tilde{u}t/d \sim 5$, at which time R_G has grown to approximately $1.5d$, the radius of gyration enters a diffusive growth regime proportional to \sqrt{t} . This is approximately the time when the horizontal diffusivity approaches a constant value as shown in Fig. 7(a). It is interesting that the timescale used here collapses the results also in the intermediate period between the ballistic and diffusive regimes. This feature must depend on the relative smallness of the velocity fluctuations compared with the mean relative velocity with respect to the liquid already found in Figs. 1 and 14.

The normalized shape eigenvalues (22) averaged over all the tetrads are shown in Fig. 16. After a short initial time $\tilde{u}t/d \sim 1$, during which the tetrads remain close to their initial shape, the normalized eigenvalues start evolving until they reach approximately steady values around $\tilde{u}t/d \sim 10$. The curves corresponding to different Galilei numbers collapse reasonably well, but not as well for different ϕ . The numerical values of the $\langle I_k \rangle$'s show that the initially regular tetrads evolve into thin elongated structures at long times. Interestingly, the same trend is found in single-phase homogeneous turbulent flow [44,47]. The author of the latter reference attributes this result to a diffusive process with a separation-dependent diffusivity in the manner of Richardson [48]. Around $\tilde{u}t/d \sim 10^2$, we begin to see a departure from the steady state that corresponds to $\langle R_G \rangle$ approaching the shortest dimension of the computational domain.

The behaviors of the shape variance Δ and shape factor S , shown in Fig. 17, are compatible with this interpretation. The asymmetry parameter Δ reaches a value of approximately 0.6, which is compatible with a very small third eigenvalue, i.e., with the particles forming a thin tetrad. The shape factor reaches a steady-state value of $S \approx 0.75$, indicating prolate shapes, as also demonstrated by the normalized eigenvalues of Fig. 16. The shape and symmetry of the tetrads remain approximately

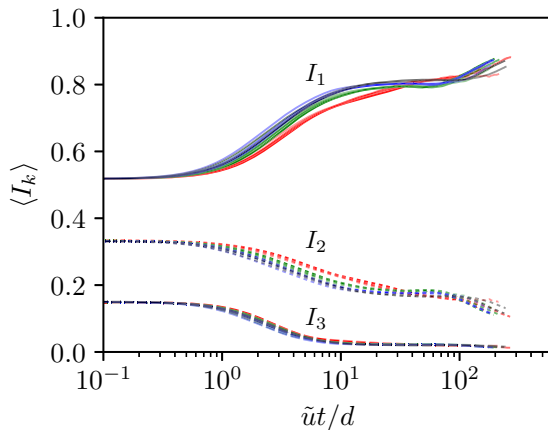


FIG. 16. Time dependence of the normalized eigenvalues of the shape tensor (22) for $\rho_p/\rho_f = 2$ (gray), 3.3 (green), 4 (red), and 5 (blue).

constant up to $\tilde{u}t/d \sim 1$. Over the following decade of time, the tetrads change shape rapidly, ultimately reaching approximately steady values around $\tilde{u}t/d \sim 10$. The appearance of all these figures changes from $\tilde{u}t/d \sim 100$ onward, probably an effect of the tetrad size approaching or exceeding the dimensions of the computational domain.

2. Shape alignment

The alignment $\mathbf{e}_z \cdot \mathbf{v}_k(t)$ of the tetrad principal axes with \mathbf{e}_z , the direction of gravity, is shown in Fig. 18. The initial value of this quantity, close to 0.5, indicates that the initialization of the tetrads is not preferentially aligned with any direction. With time, the tetrad's largest principal axis tends to become preferably aligned with gravity and the cosine of the angles that the intermediate and minor axes form with gravity decreases, indicating a tendency toward a horizontal arrangement. Up to $\tilde{u}t/d \sim 5$ –10, however, the average of $\mathbf{e}_z \cdot \mathbf{v}_k(t)$ does not deviate very much from 0.5. This effect indicates that, initially, the tetrads mostly respond to the local flow conditions, with gravity emerging only later as a dominant factor in the determination of their shape.

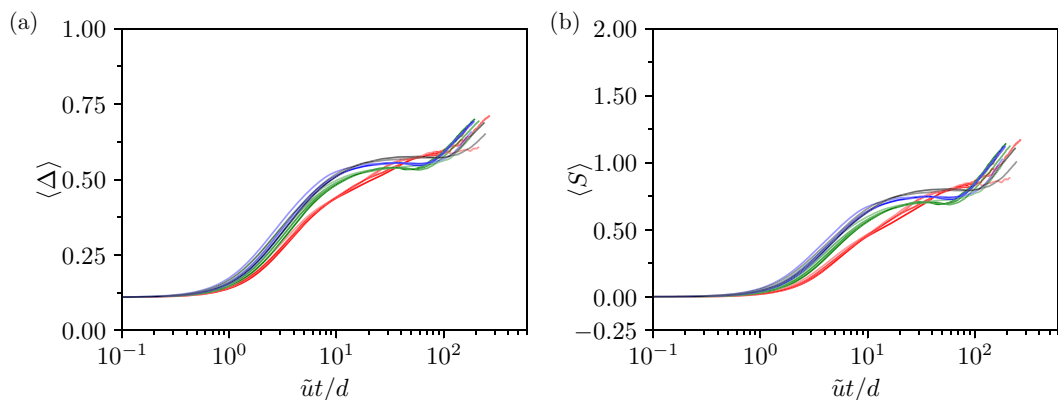


FIG. 17. Time dependence of the shape variance Δ [Eq. (24)] and shape factor S [Eq. (25)] for $\rho_p/\rho_f = 2$ (gray), 3.3 (green), 4 (red), and 5 (blue). Increasing hue saturation corresponds to increasing particle volume fraction (see the Supplemental Material [18]).

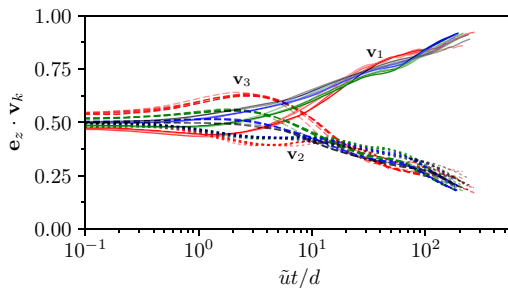


FIG. 18. Time dependence of the alignment of the tetrad principal axes with gravity. Colors refer to different particle-to-fluid density ratios $\rho_p/\rho_f = 2$ (gray), 3.3 (green), 4 (red), and 5 (blue). Increasing hue saturation corresponds to increasing particle volume fraction (see the Supplemental Material [18]).

Figure 19 shows the alignment $\mathbf{v}_k \cdot \mathbf{s}_1(0)$ of the principal shape axes with the initial principal strain axis. At initialization, the tetrad shape is uncorrelated with the local particle field strain direction and the average value of the cosine is about 0.5. As the particles in the tetrad adapt to local conditions, however, the major, intermediate, and minor principal shape axes begin to align with their respective counterparts of the principal strain axes. Comparison with Fig. 18 shows that this process occurs before the shape principal axis \mathbf{v}_1 has had a chance of aligning with gravity, which suggests that the origin of this alignment is kinematic rather than dynamic. This is another interesting point of contact with single-phase homogeneous turbulence [44]. Unlike that case, however, we found little indication of preferential alignment of the angular velocity of the tetrads with the eigenvector corresponding to the middle eigenvalue of the strain tensor. It appears therefore that analogies that we have encountered are mostly due to kinematical effects, whereas the alignment of the angular velocity depends on dynamical features specific to single-phase turbulence. Eventually, near the onset of the diffusive behavior, the principal directions and strain become unaligned as the local conditions that generated the initial strain evolve.

A consideration of Figs. 15–19 together shows the presence of three distinct phases of the tetrads’ evolution. In the first one, up to $\tilde{u}t/d \sim O(1)$, very little is happening: Over times of this length the particle move a distance of the order of their diameter and there is little evolution of their shape.

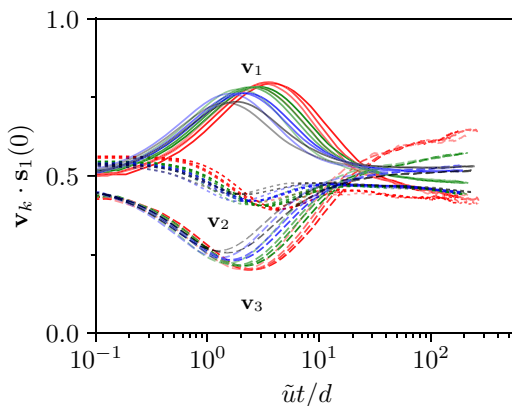


FIG. 19. Time dependence of the alignment of the tetrad principal axes with the principal rate of strain at the initial instant corresponding to the largest eigenvalue. Colors refer to different particle-to-fluid density ratios $\rho_p/\rho_f = 2$ (gray), 3.3 (green), 4 (red), and 5 (blue). Increasing hue saturation corresponds to increasing particle volume fraction (see the Supplemental Material [18]).

In a second phase, up to $\tilde{u}t/d \sim O(10)$, the complexity of the mutual interactions gradually pushes the quantities characterizing the tetrads toward an approximately steady state with prevalent stretch along the initial principal strain axis; this dynamics acquires a diffusive character under the action of the relatively small mutual disturbances. Finally, for later times, diffusion continues, but the effect of gravity becomes determinant and the principal shape axis tends to align vertically.

V. SUMMARY AND CONCLUSIONS

In this paper we have studied the settling of equal spheres suspended in an upward fluid motion extending the parameter range with respect to that used by previous investigators. By and large our results agree with previous ones for the quantities investigated earlier and the parameter ranges where there is an overlap. A feature identified in this study is the tendency toward particles clustering as revealed by the large excursions above and below the mean value of the square of the mean particle velocity fluctuations.

We have studied particle collisions, comparing the results with those of the kinetic theory of granular gases. Another feature of this work is the time evolution of tetrads, i.e., arrangements of four particles. Initially the size and orientation of the tetrads is little affected by the fluid motion, but eventually they evolve into thin, elongated structures preferentially aligned with the direction of gravity. This result is in agreement with the markedly anisotropic nature of the particle diffusivity and velocity fluctuations, which are larger in the vertical direction than in the horizontal. The transition toward an anisotropic structure occurs on the same timescale as the initial ballistic regime of the particles displacement is replaced by a diffusive regime.

It may be hoped that results of the type we have presented will foster the formulation of useful reduced descriptions of particle-fluid systems. We have taken a small step in this direction in an earlier paper [19] in which we have shown that the averaged-equation theory for kinematic waves can be recovered from the results of resolved simulations. Much work remains to be done however. The smoothening out of the statistical fluctuations of resolved simulations, while leaving the effect of the most important physical processes intact, is still an unsolved problem. For example, if an efficient and accurate method can be developed for this purpose, it will be possible to examine in detail the proposed closure relations of averaged-equation models and judge their validity. By gradually increasing the particle density with respect to that of the fluid, one may hope to gain an understanding of the nature of the instabilities affecting gas-particle fluidized beds and the manner in which these instabilities are contained in the reduced equations models. A valuable outcome of these efforts would be an understanding of the correct way in which the many nonhyperbolic reduced-description models in existence should be rendered well posed.

ACKNOWLEDGMENTS

The authors are grateful to Dr. Adam Sierakowski for his help in the course of this study and especially for his contribution to the material of Sec. IV. Simulations were run at the Maryland Advanced Research Computing Center. This work was supported by NSF under Grant No. CBET 1335965 and by the University of Houston.

-
- [1] P. N. Segre, E. Herbolzheimer, and P. M. Chaikin, Long-range correlations in sedimentation, *Phys. Rev. Lett.* **79**, 2574 (1997).
 - [2] P. N. Segre, F. Liu, P. Umbanhowar, and D. A. Weitz, An effective gravitational temperature for sedimentation, *Nature* **409**, 594 (2001).
 - [3] D. Chehata-Gomez, L. Bergougnoux, E. Guazzelli, and J. Hinch, Fluctuations and stratification in sedimentation of dilute suspensions of spheres, *Phys. Fluids* **21**, 093304 (2009).

- [4] P. Snabre, B. Pouligny, C. Metayer, and F. Nadal, Size segregation and particle velocity fluctuations in settling concentrated suspensions, *Rheologica Acta* **48**, 855 (2009).
- [5] A. Hamid, J. J. Molina, and R. Yamamoto, Sedimentation of non-Brownian spheres at high volume fractions, *Soft Matter* **9**, 10056 (2013).
- [6] W. Fornari, F. Picano, G. Sardina, and L. Brandt, Reduced particle settling speed in turbulence, *J. Fluid Mech.* **808**, 153 (2016).
- [7] J. F. Richardson and W. N. Zaki, Sedimentation and fluidisation: Part I, *Trans. Inst. Chem. Eng.* **32**, 35 (1954).
- [8] J. Garside and M. Al-Dibouni, Velocity-voidage relationships for fluidization and sedimentation in solid-liquid systems, *Ind. Eng. Chem. Proc. Des. Dev.* **16**, 206 (1977).
- [9] Y. S. Chong, D. A. Ratkowsky, and N. Epstein, Effect of particle shape on hindered settling in creeping flow, *Powder Technol.* **23**, 55 (1979).
- [10] R. Di Felice, The sedimentation velocity of dilute suspensions of nearly monosized spheres, *Int. J. Multiphase Flow* **25**, 559 (1999).
- [11] X. Yin and D. L. Koch, Hindered settling velocity and microstructure in suspensions of solid spheres with moderate Reynolds numbers, *Phys. Fluids* **19**, 093302 (2007).
- [12] E. Climent and M. R. Maxey, Numerical simulations of random suspensions at finite Reynolds numbers, *Int. J. Multiphase Flow* **29**, 579 (2003).
- [13] A. A. Zaidi, T. Tsuji, and T. Tanaka, Hindered settling velocity & structure formation during particle settling by Direct Numerical Simulation, *Proc. Eng.* **102**, 1656 (2015).
- [14] A. Hamid, J. J. Molina, and R. Yamamoto, Direct numerical simulations of sedimenting spherical particles at non-zero Reynolds number, *RSC Adv.* **4**, 53681 (2014).
- [15] R. E. Caflisch and J. H. C. Luke, Variance in the sedimenting speed of a suspension, *Phys. Fluids* **28**, 759 (1985).
- [16] E. Guazzelli and J. Hinch, Fluctuations and instability in sedimentation, *Annu. Rev. Fluid Mech.* **43**, 97 (2011).
- [17] A. J. Sierakowski and A. Prosperetti, Resolved-particle simulation by the physalis method: Enhancements and new capabilities, *J. Comput. Phys.* **309**, 164 (2016).
- [18] See Supplemental Material at <http://link.aps.org/supplemental/10.1103/PhysRevFluids.4.014304> for several additional figures that complement those shown herein, as well as two movie sequences. The first one shows the motion of 500 spheres ($\phi = 8.7\%$) with a particle-to-fluid density $\rho_p/\rho_f = 3.3$; color indicates the particle velocities. The second one is for 2000 spheres ($\phi = 34.9\%$) with the same particle-to-fluid density $\rho_p/\rho_f = 3.3$.
- [19] D. P. Willen, A. J. Sierakowski, G. Zhou, and A. Prosperetti, Continuity waves in resolved-particle simulations of fluidized beds, *Phys Rev. Fluids* **2**, 114305 (2017).
- [20] A. J. Sierakowski, GPU-centric resolved-particle disperse two-phase flow simulation using the Physalis method, *Phys. Commun.* **207**, 24 (2016).
- [21] H. Lamb, *Hydrodynamics*, 6th ed. (Cambridge University Press, Cambridge, 1932).
- [22] S. Kim, S. J. Karrila, *Microhydrodynamics: Principles and Selected Applications* (Butterworth-Heinemann, Boston, 1991).
- [23] G. Barnocky and R. H. Davis, Elastohydrodynamic collision and rebound of spheres: Experimental verification, *Phys. Fluids* **31**, 1324 (1988).
- [24] R. Clift, J. R. Grace, and M. F. Weber, *Bubbles, Drops, and Particles* (Academic, New York, 1978).
- [25] H. Nicolai, B. Herzhaft, E. J. Hinch, L. Oger, and E. Guazzelli, Particle velocity fluctuations and hydrodynamic self-diffusion of sedimenting non-Brownian spheres, *Phys. Fluids* **7**, 12 (1995).
- [26] A. J. C. Ladd, Dynamical simulations of sedimenting spheres, *Phys. Fluids A* **5**, 299 (1993).
- [27] M. Uhlmann and T. Doychev, Sedimentation of a dilute suspension of rigid spheres at intermediate Galileo numbers: The effect of clustering upon the particle motion, *J. Fluid Mech.* **752**, 310 (2014).
- [28] C. H. Rycroft, VORO ++ : A three-dimensional Voronoi cell library in C ++, *Chaos* **19**, 041111 (2009) see <http://math.lbl.gov/voro++/download/>
- [29] A. S. Sangani and A. K. Didwania, Dynamic simulations of flows of bubbly liquids at large Reynolds numbers, *J. Fluid Mech.* **250**, 307 (1993).

- [30] X. L. Yin and D. L. Koch, Lattice-Boltzmann simulation of finite Reynolds number buoyancy-driven bubbly flows in periodic and wall-bounded domains, *Phys. Fluids* **20**, 103304 (2008).
- [31] R. Zenit, D. L. Koch, and A. S. Sangani, Measurements of the average properties of a suspension of bubbles rising in a vertical channel, *J. Fluid Mech.* **429**, 307 (2001).
- [32] T. P. C. van Noije and M. H. Ernst, Velocity distributions in homogeneous granular fluids: The free and the heated case, *Granular Matter* **1**, 57 (1998).
- [33] N. V. Brilliantov and T. Pöschel, *Kinetic Theory of Granular Gases* (Oxford University Press, Oxford, 2004).
- [34] J. M. Ham and G. M. Homsy, Hindered settling and hydrodynamic dispersion in quiescent sedimenting suspensions, *Int. J. Multiphase Flow* **14**, 533 (1988).
- [35] M. A. Turney, M. K. Cheung, M. J. McCarthy, and R. L. Powell, Magnetic resonance imaging study of sedimenting suspensions of noncolloidal spheres, *Phys. Fluids* **7**, 904 (1995).
- [36] S. Chapman and T. G. Cowling, *The Mathematical Theory of Non-Uniform Gases*, 3rd ed. (Cambridge University Press, Cambridge, 1970).
- [37] X. Yin and D. L. Koch, Velocity fluctuations and hydrodynamic diffusion in finite-Reynolds-number sedimenting suspensions, *Phys. Fluids* **20**, 043305 (2008).
- [38] D. N. Theodorou and U. W. Suter, Shape of unperturbed linear polymers: Polypropylene, *Macromolecules* **18**, 1206 (1985).
- [39] J. A. Aronovitz and D. R. Nelson, Universal features of polymer shapes, *J. Phys. (Paris)* **47**, 1445 (1986).
- [40] J. Rudnick and G. Gaspari, The shapes of random walks, *Science* **237**, 384 (1987).
- [41] M. Chertkov, A. Pumir, and B. I. Shraiman, Lagrangian tetrad dynamics and the phenomenology of turbulence, *Phys. Fluids* **11**, 2394 (1999).
- [42] L. Biferale, G. Boffetta, A. Celani, B. J. Devenish, A. Lanotte, and F. Toschi, Multiparticle dispersion in fully developed turbulence, *Phys. Fluids* **17**, 111701 (2005).
- [43] H. Xu, A. Pumir, and E. Bodenschatz, The pirouette effect in turbulent flows, *Nat. Phys.* **7**, 709 (2011).
- [44] A. Pumir, E. Bodenschatz, and H. Xu, Tetrahedron deformation and alignment of perceived vorticity and strain in a turbulent flow, *Phys. Fluids* **25**, 035101 (2013).
- [45] V. G. Mavrantzas and D. N. Theodorou, Atomistic simulation of polymer melt elasticity: Calculation of the free energy of an oriented polymer melt, *Macromolecules* **31**, 6310 (1998).
- [46] J. Rudnick and G. Gaspari, The asphericity of random walks, *J. Phys. A: Math. Gen.* **19**, L191 (1986).
- [47] B. J. Devenish, Geometrical Properties of Turbulent Dispersion, *Phys. Rev Lett.* **110**, 064504 (2013).
- [48] L. F. Richardson, Atmospheric diffusion shown on a distance-neighbor graph, *Proc. R. Soc. London Ser. A* **110**, 709 (1926).